Solar Energy 212 (2020) 297–308

Contents lists available at ScienceDirect

Solar Energy

journal homepage: www.elsevier.com/locate/solener

Dynamic photogrammetry applied to a real scale heliostat: Insights into the wind-induced behavior and effects on the optical performance

Kristina Blume [a,*], Marc Röger [b], Tim Schlichting [a], Ansgar Macke [c], Robert Pitz-Paal [d]

[a] DLR, German Aerospace Center, Institute of Solar Research, Karl-Heinz-Beckurts Str. 13, 52428 Jülich, Germany
[b] DLR, German Aerospace Center, Institute of Solar Research, Paseo de Almería 73, 04001 Almería, Spain
[c] CSP Services GmbH, Friedrich-Ebert-Ufer 30, 51143 Cologne, Germany
[d] DLR, German Aerospace Center, Institute of Solar Research, Linder Höhe, 51147 Cologne, Germany

ARTICLE INFO

Keywords:
Dynamic photogrammetry
Real scale heliostat
Wind-induced behavior
Optical performance

ABSTRACT

Wind loads may decrease a heliostat's optical performance by affecting its shape and orientation. As small scale wind tunnel or numerical models cannot reflect a heliostat's dynamic behavior entirely, in this study we investigated a real scale Stellio heliostat installed on the DLR heliostat testing platform where it was exposed to the natural wind. The wind-induced response was captured with a dynamic photogrammetry system that combines a high spatial and high temporal resolution. As its application to a heliostat is novel, the first focus of this paper is to validate the applied setup and the accuracy of measured displacements. The second focus is to discuss the wind-induced Stellio behavior. A method is presented which allows for separating the total wind-induced behavior into a tracking- and a slope-relevant part. Based on this separation, the wind-induced tracking deviation (0.44 mrad RMS) during the investigated measurement period (mean wind speed ≈ 4.8 m/s, mean turbulence intensity ≈ 26 %) reached a level of approximately one third of a heliostat's typical total tracking deviation. Likewise, during the time step of largest deformations, the wind-induced slope deviation (0.75 mrad RMS) of the most affected facet reached a level of approximately one third of a Stellio facet's total slope deviation. However, wind-induced slope deviations occurred only locally and temporally. Furthermore, wind-excited eigenfrequencies were revealed to have a negligible impact on both the tracking and slope deviation in case of the Stellio. Oscillations and deformations related to frequencies below the eigenfrequencies were rather found to have a predominant impact on the optical performance.

1. Introduction

The role of a heliostat in a solar tower plant is to reflect and focus the incident solar radiation on a desired aimpoint on the receiver surface with high efficiency. However, external loads such as gravity or wind loads may decrease the efficiency by affecting the concentrator's shape or orientation. Especially the dynamic nature of wind load can lead to oscillations of the entire concentrator, to an excitation of eigenfrequencies and to deformations of the mirror facets.

Besides affecting the optical performance, wind loads have the potential to cause structural failure and a decrease in service life of heliostats. Therefore, many previous studies have focused on proper design of heliostats against wind loads. Several wind tunnel measurement campaigns and numerical studies have been conducted on isolated heliostats to determine wind load coefficients and study their dependence on different wind conditions (Peterka et al., 1989; Pfahl and Uhlemann, 2011; Gong et al., 2013; Emes et al., 2017, 2019) and on different heliostat design aspects (Wu et al., 2010; Pfahl et al., 2011). Some studies furthermore investigated the impact of dynamic wind loads and the wind-induced response of a heliostat with regard to stresses in the structure and fatigue failure (Gong et al., 2012; Vasquez Arango, 2016).

While structural failure and proper heliostat design against wind load has been studied intensively, the impact of wind load on the optical performance is yet to be investigated further. Heliostat models, such as small scale wind tunnel or numerical models are not suitable to reflect the mechanical and structural properties of a real heliostat entirely. Hence, experimental investigations on real scale heliostats are vital to detect phenomena that may have significant impact on the optical performance, such as local deformations of the mirror facets.

One approach to study wind effects on the optical performance of a real scale heliostat was presented by Griffith et al. (2015) and Ho et al. (2012). Amongst other sensors, in their study a Sandia CRTF testbed heliostat was equipped with accelerometers in order to conduct a hammer-excited experimental modal analysis and a wind-excited

* Corresponding author.
E-mail address: kristina.blume@dlr.de (K. Blume).

https://doi.org/10.1016/j.solener.2020.10.056
Received 3 July 2020; Received in revised form 12 October 2020; Accepted 18 October 2020
Available online 25 November 2020

Nomenclature

r	Cylindrical coordinate, radial direction of heliostat concentrator (m)
x	Cartesian coordinate, horizontal direction of heliostat concentrator (m)
y	Cartesian coordinate, vertical direction of heliostat concentrator (m)
z	Cartesian or cylindrical coordinate, direction of optical axis of heliostat concentrator (m)
2D	Two-dimensional
3D	Three-dimensional
ACC	Acceleration
EMA	Experimental modal analysis
EVAL	Evaluated point cloud
PG	Photogrammetry
REF	Reference point cloud
RMS	Root mean square
SD	Slope deviation
α	Azimuth angle (°)
φ	Cylindrical coordinate, angular direction of heliostat concentrator (°)
γ	Elevation angle (°)
$\Delta SD_{rad,wind}$	Wind-induced slope deviation in radial direction (mrad)
$\Delta SD_{tan,wind}$	Wind-induced slope deviation in tangential direction (mrad)
$\Delta Track_{x,wind}$	Wind-induced tracking deviation about x-axis (mrad)
$\Delta Track_{y,wind}$	Wind-induced tracking deviation about y-axis (mrad)
2σ	Coverage factor of measurement precision (95.45%)

operational modal analysis. During the wind-excited campaign, the heliostat was exposed to the natural wind. Griffith and Ho revealed that eigenmodes, especially out-of-plane bending modes, impact the beam quality and thus affect the optical performance. Additionally, they noticed a significantly higher damping behavior during the wind-excited tests and concluded that the total damping behavior is comprised of a structural damping component and, to a large extend, of an aerodynamic damping component. Griffith's and Ho's findings emphasize (1) the impact of wind loads on the optical performance of heliostats and (2) the need of conducting measurements on real scale heliostats to study their true wind-induced behavior.

As aforementioned, the experimental investigations by Griffith and Ho were based on accelerometers. This is a reasonable choice when investigating eigenfrequencies. However, accelerometers have the drawback of not resolving very low frequencies sufficiently. Yet, investigations on buildings and structures under wind load indicated that significant wind-induced deformations and oscillations appear in the very low frequency range (up to approximately 1 Hz), below the typical first eigenfrequency of such structures (Holmes, 2015). Therefore, in this work a new measurement system is introduced which is specifically capable of resolving the very low frequency range. For the first time, a dynamic photogrammetry system is applied to a heliostat in order to study its wind-induced dynamic behavior. The investigated heliostat is a Stellio heliostat, invented by sbp sonne GmbH, and installed on the DLR heliostat testing platform in Jülich, Germany. Besides resolving the very low frequency range, the dynamic photogrammetry system offers the great advantage of combining a high spatial and a high temporal resolution at the same time which allows for novel insights into the dynamics of a real scale heliostat under wind load.

The paper is organized as follows. In Section 2, the theoretical background is introduced that is of importance in the framework of this study while in Section 3, the applied experimental setup is explained. As one aim of this study is to validate the applied dynamic photogrammetry setup and the accuracy of measured displacements, Section 4 will present the validation process. The second aim of this study is to provide an insight into the wind-induced dynamic behavior of a Stellio heliostat and to investigate effects on the optical performance which will be discussed in Section 5. Finally, a summary and conclusion is given in Section 6.

2. Theoretical background

The wind-induced behavior of buildings and structures has been investigated thoroughly in the past and the detected patterns may be applicable to heliostats as well. To examine this in the presented work, a common classification of wind-induced behavior is introduced in the following as it is used in the field of structural dynamics. Furthermore, as this paper will investigate the impact of wind load on the optical performance of a heliostat, definitions of wind-induced deviations will be given in this section. In addition, the measurement principles and constraints of a photogrammetry system will be explained that are of relevance in the framework of this paper.

2.1. Structures under wind load

In Holmes (2015), the total response of a structure to wind load is described as a superposition of three components, i.e. the mean, the background and the resonant component. The mean response appears as a static displacement caused by a constant wind load due to the mean approaching wind speed. Additionally, slow changes in wind speed lead to slow oscillations of the structure. This behavior is termed background response and comprises all oscillations of lower frequencies than the first eigenfrequency of the structure. Furthermore, the turbulent nature of wind excites the structure's eigenfrequencies leading to additional oscillations. Such behavior is named resonant response and consequently comprises all oscillations of higher frequencies. However, in Holmes the resonant response component is described as negligible for most structures compared to the mean and background response component. If this is the case for heliostats as well, particularly the Stellio heliostat, will be discussed in Section 5.

2.2. Heliostat performance assessment

As wind loads have the potential to affect a heliostat's shape and orientation, this paper specifically relates to aspects of the optical performance of a heliostat. More precisely, not the entire heliostat but its concentrator is taken into account which is the tracking mirror assembly that reflects the sunlight towards the receiver. Regarding the effects of wind load on the optical performance, two wind-induced deviations are of special interest in the framework of this paper. Wind-induced changes in the orientation of the concentrator are considered by means of a tracking deviation while the impact of wind load on the concentrator shape is represented by a mirror slope deviation. The determination of tracking and mirror slope deviations requires a coordinate system which is defined as shown in Fig. 1. The z-axis is assigned to the optical axis of the concentrator while the x-axis is defined horizontally. Additionally, the desired orientation of the concentrator is described by its elevation angle γ and azimuth angle α, defined as shown in Fig. 1.

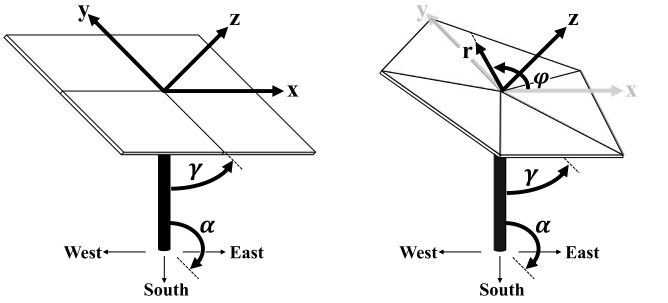

(a) Cartesian coordinates for rectangular concentrator shapes

(b) Cylindrical coordinates for (approximate) rotationally symmetric concentrator shapes

Fig. 1. Definition of heliostat coordinate systems and azimuth angle α and elevation angle γ.

2.2.1. Tracking deviation

The tracking deviation in the framework of this paper is defined as the angular deviation between the concentrator's actual orientation (i.e. the direction of its optical axis) from its desired orientation. Deviations of the orientation occur for example due to wear of the gears, the motor control system or due to external loads such as gravity or wind (Heller, 2017). The overall resulting deviation is termed total tracking deviation. On the other hand, such deviation that is solely caused by wind load and wind-induced oscillations, is called wind-induced tracking deviation and will be investigated in the framework of this paper. Corresponding to an angular deviation about the x- and *y*-axis, the wind-induced tracking deviation is termed $\Delta Track_{x,wind}$ and $\Delta Track_{y,wind}$ and is given in the unit mrad. As the wind-induced tracking deviation is of highly dynamic nature, instantaneous values and time averages must be distinguished. In the framework of this paper, the root-mean-square (RMS) value as a statistical measure is determined from the temporal tracking deviation courses.

2.2.2. Mirror slope deviation

In contrast to the tracking deviation that accounts for the concentrator's orientation solely, the mirror slope deviation (short: slope deviation) solely accounts for the shape of the concentrator. The slope deviation is caused by a deviation of the actual shape from the ideal shape for example due to canting and contour errors or due to temperature gradients, gravity or wind load (Röger et al., 2017). The overall resulting angular deviation is termed total slope deviation. It is a spatially resolved measure over the investigated facets and is typically defined in x- and *y*-direction (Fernández-García et al., 2017) or, in cases of (approximate) rotationally symmetric concentrator shapes like the Stellio concentrator, in radial and tangential direction.

A slope deviation which can solely be traced back to wind load and wind-induced deformations, is called wind-induced slope deviation and is evaluated in the framework of this paper. It is defined in radial and tangential direction, termed $\Delta SD_{rad,wind}$ and $\Delta SD_{tan,wind}$ and is given in the unit mrad. Analogously to the wind-induced tracking deviation, the wind-induced slope deviation is of highly dynamic nature and instantaneous values and time averages must be distinguished. In addition and due to the spatial resolution of the slope deviation, not only time averages but also spatial averages may be determined from the instantaneous values. In the framework of this paper, the instantaneous values and spatial averages in terms of RMS values are evaluated.

2.3. Photogrammetry measurement principle

A photogrammetry system (PG system) is used to determine a three-dimensional (3D) model of a structure's geometry by taking photos of the structure from several different perspectives. Especially for the investigation and 3D assessment of large scale solar concentrators, a PG system has been proven a flexible, accurate and widely utilized measurement tool (Pottler et al., 2004, 2011).

The structure to be investigated (e.g. a solar concentrator) is equipped with adhesive, retro-reflective stickers, called targets, that define the 3D model grid points and can be precisely identified in each photo. A few targets contain a unique code, called coded targets, and allow the orientation of all photos to one another. From a set of photos the positions of all targets are then reconstructed and a point cloud with 3D coordinates results, representing the structure's geometry. A coordinate system is defined by mounting a reference cross to the structure which is equipped with coded targets that determine two spatial directions of a cartesian coordinate system. Additionally, scaling rods are attached to the structure that are equipped with targets of known distances to set the scale of the model.

A set of photos can be generated by using a single camera and taking photos consecutively or by utilizing multiple cameras (permanently installed or mobile) to take photos simultaneously. The latter concept is accomplished by a multi-camera photogrammetry system and is used to study dynamic effects of structures. Hence, it is sometimes referred to as a dynamic photogrammetry system (dynamic PG system). While numerous photos of a static subject can be taken consecutively with a single camera PG system, the number of photos in case of a dynamic PG system is limited to the number of applied cameras to capture the dynamic subject at each time step. When using four cameras, as it will be the case during this study, the available amount of photos per set (four) is not sufficient to reconstruct the structure's geometry without providing additional information. Therefore, a pre-calibration of the cameras is required using a calibration board that contains targets of known positions. This step is called inner calibration of the cameras and usually remains valid as long as the cameras are not modified (e.g. changing the lens).

Additionally, when using mobile cameras that can be positioned individually for each measurement setup, as it will be the case during this study, a second preparatory step is required prior to a dynamic PG measurement. A pre-measurement of the structure to be investigated must be conducted with a single camera PG system to provide ground control points to the evaluation routine of the dynamic PG system. The pre-measurement remains valid until the target positions (ground control points) change.

Regarding the accuracy of a dynamic PG system, the reduced number of photos per set, amongst other factors, leads to a relatively low accuracy of absolute position (coordinate) measurements compared to a single camera PG system. Yet, the accuracy of deformation or displacement measurements of a dynamic PG system is high. While the absolute position accuracy is significantly influenced by systematic errors of the PG system, the difference between two absolute positions, i.e. a displacement, is almost unaffected (Albert et al., 2002). Also, the precision of a dynamic PG system, i.e. the scattering of a target's measured position over time, is sufficiently high as will be further discussed in the following section and in conclusion a dynamic PG system is well suited to study the dynamics of a structure.

3. Experimental setup

In this study, the wind-induced behavior of a Stellio heliostat was captured with a dynamic PG system to investigate the impact of wind load on a real scale heliostat. Simultaneously to the dynamic PG measurements, the approaching wind speed was measured with four ultrasonic anemometers. Details on the measurement systems as well as on the Stellio heliostat and its installation on the DLR heliostat testing platform are given in the following.

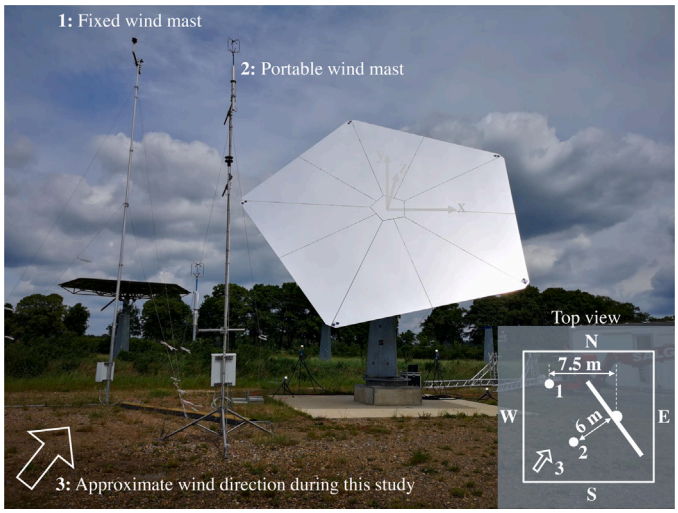

Fig. 2. Stellio heliostat installed on the DLR heliostat testing platform and arrangement of wind measurement equipment. Note that the Stellio was differently oriented during measurements of this study. The applied azimuth and elevation angles are presented in Tables 4 and 5.

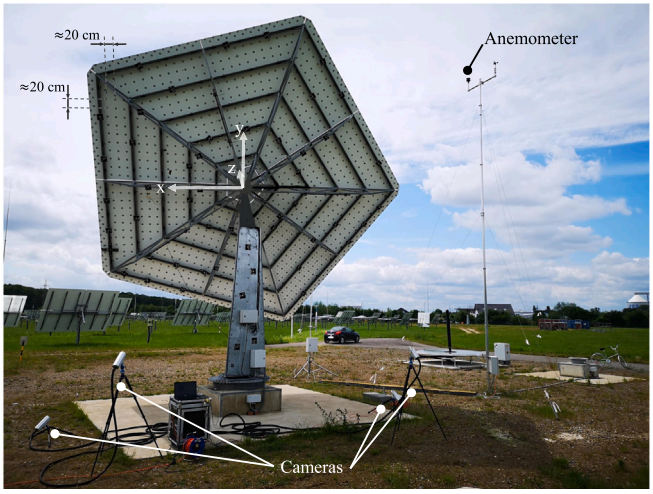

Fig. 3. Exemplary setup of the dynamic photogrammetry system with cameras mounted to tripods. The applied camera setup during this study is shown in Fig. 4. Furthermore, note that the Stellio was differently oriented during measurements of this study. The applied azimuth and elevation angles are presented in Tables 4 and 5.

3.1. Stellio heliostat and heliostat testing platform

The Stellio heliostat, shown in Fig. 2, was developed by sbp sonne GmbH together with partners Ingemetal and Masermic. It has a reflective area of approximately 48.5 m^2 and differs from other heliostats in terms of its pentagon-shaped concentrator, improved optical quality and inclined drive axle using linear actuators (Balz et al., 2016; Arbes et al., 2016). For the purpose of long-term performance evaluation and thorough testing during this and other studies (e.g. Nieffer et al. (2019)), the Stellio was installed on the heliostat testing platform (HeliTep), as shown in Fig. 2, at the DLR site in Jülich. Amongst other advantages, the HeliTep provides optimal conditions for wind studies on a single real scale heliostat as the installed heliostat is exposed to the natural wind without significant disturbances in the close vicinity for wind directions between south-west, west and north-west.

Table 1
General specifications of the dynamic photogrammetry system.

Number of cameras	4
Camera type	IDS UI-3080CP-M-GL Rev.2
Camera resolution	5 megapixel
Sample rate (max.)	50 Hz
Precision (declared)[1]	0.15 mm (2σ)
Precision (typical)[1]	0.04–0.1 mm (2σ)

Table 2
Specifications and settings of dynamic photogrammetry measurements conducted during this study.

Used number of cameras	4
Applied sample rate	30 Hz
Number of applied targets	≈ 1200
Target diameter	40 mm
Expected PG data precision	0.04–0.1 mm (2σ)

3.2. Dynamic photogrammetry system

Dynamic PG systems are used in a number of applications but have never been applied to study the dynamics of a heliostat. Therefore, a suitable dynamic PG system was acquired from the company Linearis3D and for the first time applied to the Stellio. The general specifications and limitations of the dynamic PG system as well as the specific settings during measurements of this study are presented in the following.

3.2.1. General specifications and limitations

Table 1 summarizes the specifications of the dynamic PG system. Regarding the precision, the manufacturer declares a precision of at least 0.15 mm under laboratory conditions.[1] During our own tests under laboratory conditions, we found the precision to be typically in a range of 0.04–0.1 mm, being positively affected by

- a high number of camera observations per target. The maximum of four camera observations is aspired.
- an angle between two camera viewing directions close to 90°.
- a short distance between cameras and targets.
- a rigid camera fixation. The cameras must be prevented from moving or oscillating.

The maximum acquisition time of the dynamic PG system is limited by the RAM memory of the measurement computer as the captured photos must be temporarily stored during a measurement. By lowering the sample rate, the maximum acquisition time can be increased. In case of the measurement computer of this study, for example a sample rate of 30 Hz allows a feasible acquisition time of about 180 s.

Fig. 3 demonstrates an exemplary setup of the dynamic PG system at the Stellio heliostat with all four cameras mounted to tripods that can be adjusted in height.

3.2.2. Study-specific settings

The specifications and settings of the dynamic PG measurements conducted during this study are summarized in Table 2. The precision is expected to be in the order of magnitude as the typical precision that had been found during laboratory tests, see Section 3.2.1.

Fig. 4 demonstrates the applied camera setup where all four cameras are mounted as close to the ground as possible to keep the impact of wind on the cameras as low as possible. The cameras were positioned in a way that only the lower half of the Stellio concentrator was captured to keep a short distance between cameras and targets in favor of the precision. The required camera pre-calibration, mentioned in

[1] Precision of dynamic PG system is defined under laboratory conditions. Setup: 2 × 2 m target wall with 20 mm retro-reflective targets, 2 × 2 m square arrangement of cameras, 3 m distance between cameras and target wall.

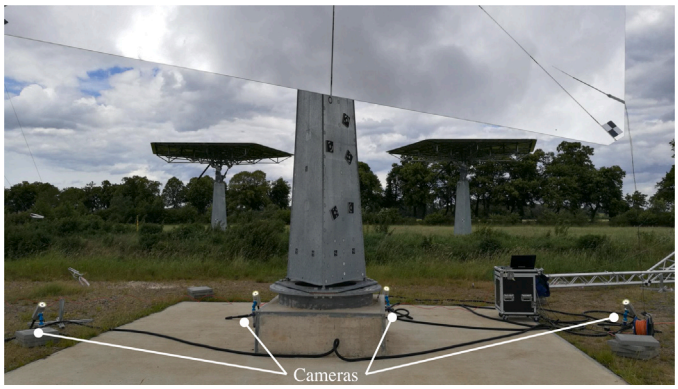

Fig. 4. Applied setup of the dynamic photogrammetry system during measurements of this study.

Table 3
Anemometer specifications and mounting setup.

Anemo-meter	Wind-field	Mounting height in m	Sample rate in Hz	Wind-mast
1[a]	3D	≈ 3	20	Portable
2[b]	2D	≈ 5	4	Portable
3[a]	3D	≈ 7	20	Portable
4[b]	2D	≈ 10	4	Fixed

[a]Gill Instruments *WindMaster* 1590-PK-020/W.
[b]Gill Instruments *WindSonic* Option 1 1405-PK-021.

Section 2.3, had been conducted prior to the presented study by using a calibration board acquired from the manufacturer. The necessary pre-measurement of the Stellio heliostat was conducted with the single camera PG system *DPA Professional* from the company Hexagon (former Aicon).

3.3. Ultrasonic anemometers

At the DLR HeliTep, in total four ultrasonic anemometers are mounted on two separate wind masts to conduct wind studies and measure the wind speed which approaches the installed heliostat. One wind mast is permanently installed and one is portable, see Fig. 2. Table 3 provides information on the anemometer specifications and their mounting. During this study, the portable wind mast was positioned south-westward of the Stellio heliostat as shown in Fig. 2 with respect to the prevailing wind direction (south-west). The specific wind conditions during the measurement periods of this study are stated in Section 4.1 and in Table 5. In order to record photogrammetry data and wind data synchronized in time, the wind data logger was connected to the computer which ran the photogrammetry software to ensure that both measurement systems referred to a common time.

4. Validation of dynamic photogrammetry setup

Since the dynamic PG system has been used for the first time to investigate a real scale heliostat under wind load, the reliability and quality of the measurement data in consideration of the applied camera setup had to be investigated. Referring to the list of factors that impact the precision, given in Section 3.2.1, three aspects of the applied measurement setup at the Stellio heliostat were identified to be of special importance:

- Due to masking effects of the structure or the pylon, some targets may not be captured by the aspired maximum number of four cameras.
- The distance between cameras and targets (i.e. the Stellio concentrator) and the total area of the concentrator to be captured is a compromise.
- The cameras are exposed to the natural wind and therefore a rigid fixation may not always be assured.

4.1. Validation process

The measurement quality of the dynamic PG system is evaluated in two steps, both based on the same dynamic PG measurement period during which the Stellio was excited by the natural wind (length of measurement period: ≈ 165 s, mean wind speed: ≈ 3.7 m/s, mean turbulence intensity: ≈ 31%). The camera setup was (nearly) identical to the one shown in Fig. 4. In a first step, see Section 4.2, dominant frequencies extracted from the dynamic PG measurement are compared to eigenfrequencies of the Stellio that have been determined through an experimental modal analysis.[2] In this way it is possible to reveal frequencies contained in the dynamic PG data that cannot be assigned to heliostat oscillations and thus might result from camera oscillations. In a second step, see Section 4.3, the PG measured displacement of one single target is compared to a redundant displacement measurement of the same target but obtained from simultaneous acceleration measurements.

4.2. Comparison of dominant frequencies

To extract dominant frequencies from dynamic PG data, in a first step the amplitude spectra[3] from the displacement time series of each single target are determined, separated by the coordinates x, y and z. As peaks in the amplitude spectra of a single target are difficult to distinguish due to the appearance of noise, in a second step the amplitude spectra of all targets are averaged to receive a mean amplitude spectrum for each spatial direction. The advantage of mean amplitude spectra is that truly dominant frequencies add up while noise cancels out. The result of this process is shown in Fig. 5 and reveals distinctive peaks in the frequency domain, referred to as dominant frequencies in this paper. As eigenfrequencies, due to their amplifying effect when excited, occur as distinctive peaks in the frequency domain, the dominant frequencies can be assigned to eigenfrequencies of the Stellio. However, in case of imperfectly fixed cameras, peaks in the frequency domain might also indicate camera oscillations. In Fig. 5, eigenfrequencies are expected only in the frequency range above 2 Hz which corresponds to the resonant response of the Stellio. Therefore, the frequency range below 2 Hz is not evaluated and is grayed out. Table 4 lists the dominant frequencies extracted from Fig. 5 in the right column and true eigenfrequencies of the Stellio, obtained from an experimental modal analysis[2] (EMA), in the left column. Additionally, the orientation of the Stellio during both measurements is listed. A differing orientation can explain minor deviations between the dominant frequencies and the eigenfrequencies.

In Table 4, the dominant frequencies between 2 and 4 Hz match the eigenfrequencies of the Stellio heliostat well, except for the frequency 3.25 Hz which corresponds to a minor peak in Fig. 5. Most likely this exceptional peak does not indicate camera oscillations but rather results from the highly dynamic interaction between the Stellio heliostat and the wind excitation. In the frequency range between 7 and 8 Hz, the eigenfrequency of 7.06 Hz is not assignable to a dominant frequency while the eigenfrequency of 7.83 Hz is assignable. However, the corresponding peak in Fig. 5 is very small. The non-assignable eigenfrequency of mode no. 4 and the small peak of mode no. 5 indicate that the eigenfrequencies between 7 and 8 Hz were almost not excited or the amplitudes of the Stellio movement were

[2] The EMA was conducted by DLR using Brüel&Kjaer measurement equipment: 11 acceleration sensors with a sensitivity of 100 mV/g and an impact hammer with a sensitivity of 0.225 mV/N.

[3] The amplitude spectra are determined from power spectra, estimated by using Matlab's *pwelch* function with default settings.

Table 4
Comparison of Stellio eigenfrequencies obtained from an experimental modal analysis (EMA) and dominant frequencies extracted from a dynamic photogrammetry measurement.

	EMA (Eigenmode No.)	Dynamic PG measurement	
Azim.	200°	140°	
Elev.	30°	30°	
Frequency in Hz	2.22 (1)	2.27	(Mostly) matching
	-	3.25	
	3.33 (2)	3.44	
	3.53 (3)	3.63	
	7.06 (4)	-	(Mostly) not assignable
	7.83 (5)	8.00	
	-	9.73	
	-	9.94	
	11.59 (6)	11.97	Not clearly assignable
	11.65 (7)	12.13	
	11.72 (8)	12.33	

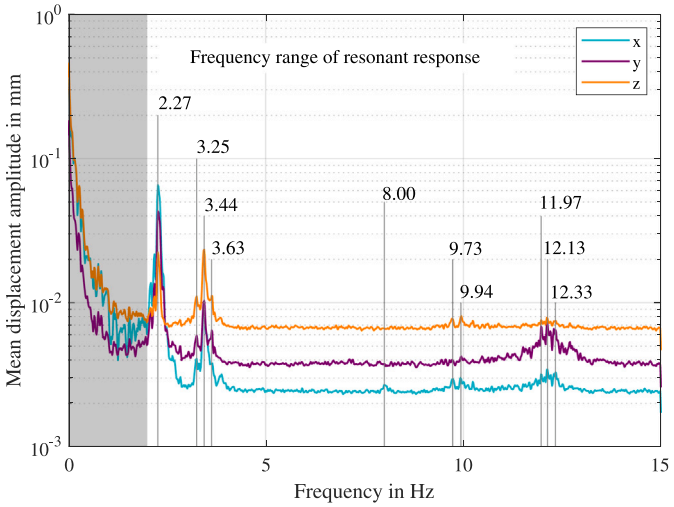

Fig. 5. Mean displacement amplitude spectra determined from the amplitude spectra of all targets to identify dominant frequencies contained in dynamic photogrammetry data. Dominant frequencies can be assignable to eigenfrequencies of the Stellio which are expected in the range above 2 Hz, corresponding to the resonant response. Therefore, the range below 2 Hz is not evaluated and is grayed out.

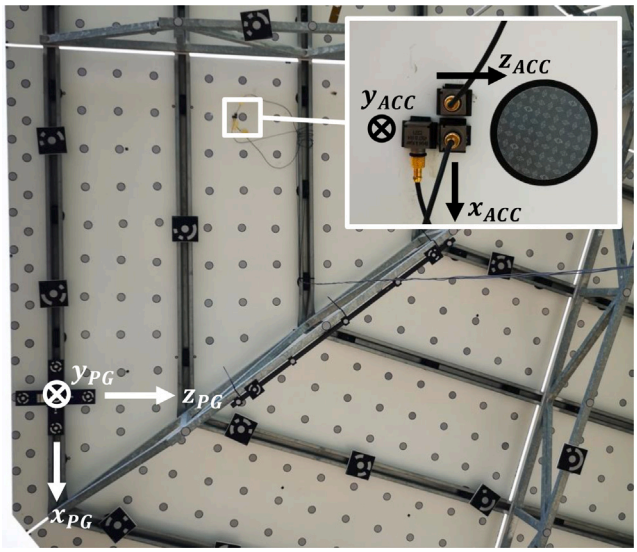

Fig. 6. Definition of dynamic photogrammetry and acceleration sensor coordinate systems and application of acceleration sensors for redundant displacement measurements. This definition of coordinate systems is only applicable during this Section 4.3.

not well resolvable due to precision limitations. Lastly, the dominant frequencies and the eigenfrequencies between 9 and 13 Hz are either not assignable or not clearly assignable. This observation indicates camera oscillations. However, the corresponding peaks in Fig. 5 are of minor degree compared to the well matching peaks between 2 and 4 Hz.

The aforementioned observations lead to the following main conclusions:

- Frequency range below 4 Hz: The Stellio movement is resolvable and the dynamic PG data is considered plausible. In particular, the data is considered plausible despite the occurrence of minor camera oscillations, appearing in the frequency range above 4 Hz.
- Frequency range above 4 Hz: The Stellio movement is either not well resolvable or minor camera oscillations lead to false, yet minor displacements. In the framework of this paper, the frequency range above 4 Hz will not be considered nor evaluated due to aforementioned reasons.

4.3. Comparison of redundant displacement measurements

In the second validation step, the accuracy of PG measured displacements is evaluated. Therefore, the measured displacement of a single target is compared to a redundant displacement measurement obtained from acceleration measurements. Three uniaxial acceleration sensors[4] were placed next to a PG target in such a way that the spatial directions of both measurement systems were in accordance, see Fig. 6. For convenience, the measurement data of this validation step is not transformed to the concentrator coordinate system shown in Fig. 1 but kept in its initial coordinate system (Fig. 6). By integrating the acceleration data twice, a redundant displacement time series resulted. During the measurement period, the target was captured by only two cameras of the dynamic PG system, i.e. the two right cameras shown in Fig. 4. Hence, this validation step assesses the accuracy of PG measured displacements under least favorable conditions.

The simultaneously and redundantly measured displacements of the investigated target are compared and analyzed in frequency domain. Fig. 7 depicts the amplitude spectra obtained from the PG data (in the following named PG amplitude spectra) and from the integrated acceleration data (in the following named ACC amplitude spectra). The gray shaded areas represent the expected lower limit of the dynamic PG data precision, see Section 3.2.2, and therefore indicate the expected limit of the PG system to resolve Stellio movements. Furthermore, the frequency range below 2 Hz is not shown and not compared as

[4] Brüel&Kjaer uniaxial acceleration sensors with a sensitivity of 100 mV/g.

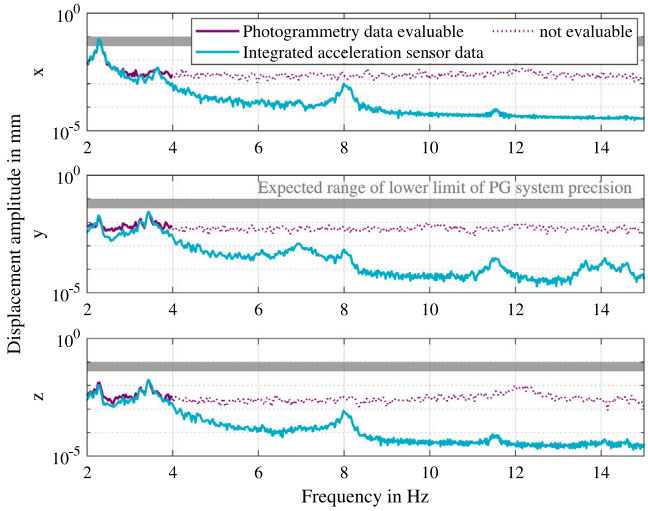

(a) Frequency range between 2 and 15 Hz. Photogrammetry data above 4 Hz is not evaluated due to the conclusions of the previous validation step, see section 4.2. Frequency range below 2 Hz is not displayed because acceleration sensors cannot capture very low frequencies sufficiently.

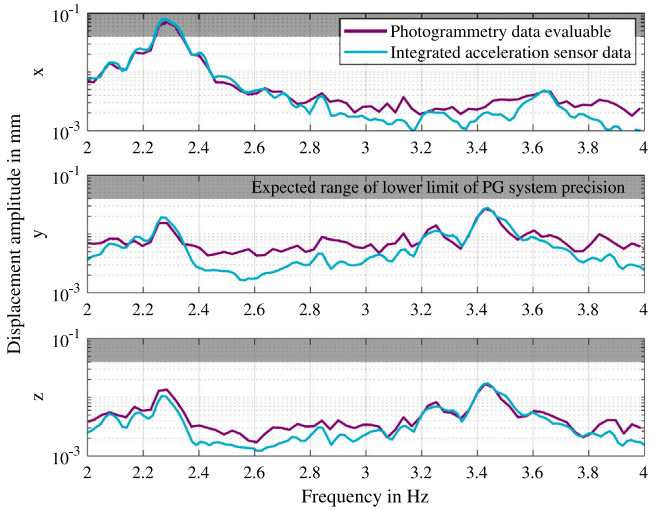

(b) Detailed view of the comparable frequency range between 2 and 4 Hz.

Fig. 7. Comparison of displacement amplitude spectra calculated from dynamic photogrammetry and acceleration sensor measurements. Gray shaded areas represent the expected lower limit of the dynamic PG data precision and indicate the expected limit of the PG system to resolve Stellio movements.

acceleration sensors cannot capture very low frequencies sufficiently enough. The PG amplitude spectra above 4 Hz are displayed dashed and, in addition, will not be compared with regard to the explanations and conclusions of the previous validation step. Yet, the ACC amplitude spectra above 4 Hz verify the previously drawn conclusion that amplitudes of the Stellio movement above 4 Hz were too small to be resolved by the dynamic PG system. The ACC amplitude spectra reveal distinctive peaks above 4 Hz that are more than one to two order of magnitudes smaller than the expected precision of the dynamic PG system and hence prove that the Stellio movement was not resolvable. The remaining and comparable frequency range is between 2 and 4 Hz. Within this range, the peaks of the PG and ACC amplitude spectra agree well. Thus, the accuracy of PG measured displacements is sufficiently high, taking into account that the Stellio amplitudes are in the same order of magnitude as the precision limit. Larger amplitudes as they are assumed to occur within the very low frequency range, below the range of eigenfrequencies, are expected to be resolved even more accurately.

The conclusions from the second validation step are drawn as follows:

- When using a camera setup as the one during this study, the accuracy of displacement measurements and the precision of the dynamic PG system is sufficiently high to study wind-induced Stellio oscillations of frequencies up to 4 Hz. In particular, the precision and accuracy is sufficiently high under least favorable conditions, i.e. only two camera observations per target.
- Minor camera oscillations, as they have been concluded during the previous validation step, do not notably affect the accuracy of displacement measurements nor the precision of the dynamic PG system.

5. Results and discussion

In this section, the wind-induced Stellio behavior captured with the dynamic PG system is studied and discussed. Therefore, Section 5.1 firstly summarizes the scope of the investigation and explains boundary conditions that need to be taken into account for the evaluation process. Then, the wind-induced behavior of the Stellio is qualitatively studied and compared to previous findings regarding structural behavior under wind load, as described in Section 2.1. Lastly, the impact of wind load on the optical performance is quantitatively analyzed, based on the explanations in Section 2.2.

Table 5
Wind conditions at approximately 6 m height and Stellio orientation during the investigated measurement period.

Mean wind speed	≈ 4.8 m/s
Mean turbulence intensity	≈ 26%
Mean wind direction	≈ 236° (west–south-west)
Elevation angle	45°
Azimuth angle	160°

5.1. Scope of investigation and boundary conditions

The validation process in Section 4 proved the applicability of the dynamic PG system and setup to study wind-induced effects of the Stellio. The results presented in this section are based on a different measurement period than used for the validation process. Yet, the same camera setup was applied and the conclusions of the validation process remain valid. The measurement period to be evaluated in this section was sampled with 30 Hz and has a total length of 165 s which is close to the maximum possible acquisition time of the dynamic PG system when sampling with 30 Hz, see Section 3.2.1.

The validation process revealed that amplitudes of frequencies above 4 Hz are not resolvable when investigating the Stellio with the applied camera setup of this study. Therefore, in preparation for analyzing the results, the PG data was filtered[5] using a lowpass filter with a cutoff frequency of 4 Hz.

Furthermore, the presented results and drawn conclusions in this section must be evaluated in consideration of the prevailing wind conditions and the heliostat orientation during the measurement period. Therefore, Table 5 states the Stellio orientation and summarizes the wind conditions during the presented measurement period.

Regarding the evaluation of wind-induced effects by means of a dynamic PG measurement and its resulting 3D point clouds, the accuracy potential of the dynamic PG system must be taken into account. While

[5] To prepare the data for filtering, missing values of a target's temporal course had to be interpolated. In this regard, a maximum number of 2 consecutive missing values were allowed. Targets with more consecutively missing values were rejected.

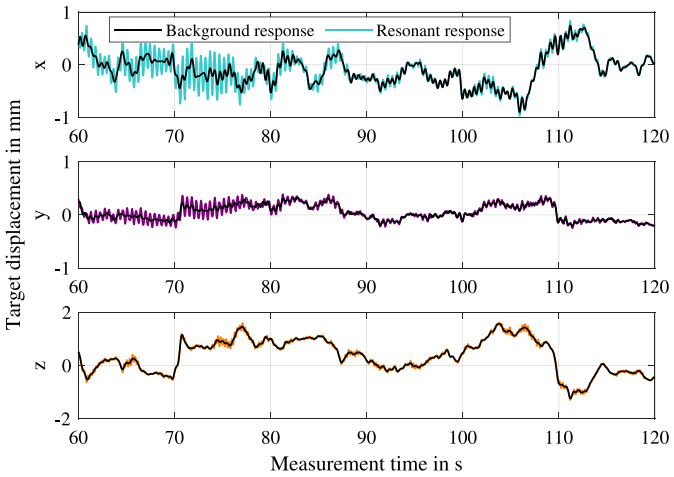

Fig. 8. Displacement time course of a single target revealing the background and resonant response of the Stellio concentrator to wind load. The background response is comprised of frequencies below 2 Hz.

displacements and deformations (the movement of the concentrator) can be accurately determined from the point clouds, the absolute shape and orientation of the concentrator is not determinable due to a relatively low accuracy of absolute position measurements, see Section 2.3. Hence, a reference point cloud must be defined that is considered wind-unaffected and which determines the reference for a displacement and deformation analysis. During this study, the reference point cloud is determined from a mean of several point clouds corresponding to the measurement period of lowest wind speed (range: 94.5–95.5 s; mean wind speed: 3.1 m/s), assuming that the concentrator was least deformed and deviated from its true resting position during such period. All results presented during this section will be referenced to aforementioned point cloud.

5.2. Qualitative assessment of wind-induced heliostat behavior

Fig. 8 depicts the measured displacement of a single target which was placed on the outermost corner of a mirror facet. An exemplary period of 60 s is presented which is taken from the full 165 s measurement. The black curves result from filtering each displacement course with a lowpass filter and a cutoff frequency just below the first eigenfrequency of the Stellio (2 Hz). As Fig. 8 reveals, the wind-induced Stellio behavior can be described as a superposition of slow oscillations, represented by the black curves, and of oscillations of higher frequencies which coincide with the range of eigenfrequencies. With regard to Section 2.1, these two types of oscillations correspond to the background and resonant response and hence, the Stellio responds similarly to wind load as structures do in general.

In more depth, the wind-induced Stellio behavior can be studied by visualizing the 3D point clouds of different time steps. Therefore, in the upper part of Fig. 9, the point clouds, and thus the concentrator shapes, of three exemplary time steps are visualized while the simultaneously measured wind speeds are depicted in the lower-most part. While the concentrator shapes within the first row of Fig. 9 represent the total behavior of the concentrator as it was captured during the measurement, the shapes of the second and third row result from a separation process of the total shapes which will be explained in the following. Note that all depicted point clouds have been scaled from real life scale of the Stellio concentrator to a scale where deformations become visible. Therefore, the axes have a unit of mm rather than m. Furthermore, the coloring of the shapes does not refer to specific values but is supposed to accentuate the concentrator's deformations and deviations solely. The time series of total shapes (first row) illustrates that the Stellio concentrator is oscillating in a stiff manner where the entire concentrator rotates as a whole. Such stiff behavior causes a tracking deviation and hereafter will be named tracking-relevant behavior. Additionally, the total shapes indicate deformations of the mirror facets which cause slope deviations. In the following, such behavior will be named slope-relevant behavior. In this regard, it must be pointed out that strong deformations, e.g. along the outermost corners and edges of a facet, are strong enough to be resolved while weaker deformations are in the same order of magnitude as noise of the dynamic PG system. For future investigations, the noise can be reduced e.g. by placing the cameras closer to the concentrator, focusing on a smaller region.

In order to study the wind-induced tracking- and slope-relevant behavior in detail, a method was developed to separate the total concentrator shape into its tracking- and slope-relevant part by means of a transformation. During the transformation process, each 3D point cloud is firstly fitted onto the reference point cloud, see Section 5.1, using a least squares method. The result of aforementioned fit is a rotation matrix and a translation vector for each point cloud (i.e. for each time step). Secondly, each point cloud is transformed by using its individual rotation matrix and translation vector. In this way, the stiff and tracking-relevant behavior of the concentrator is filtered out while the "soft" and slope-relevant behavior remains. The resulting separated tracking- and slope-relevant concentrator shapes are displayed in Fig. 9, second and third row. Based on this separation, the wind-induced tracking- and slope deviations can be determined which will be presented in the following.

5.3. Quantitative assessment of wind-induced heliostat behavior

Building up on the preceding qualitative assessment, in this section the wind-induced Stellio behavior is quantitatively assessed in terms of its wind-induced tracking and slope deviation.

5.3.1. Impact of wind load on tracking deviation

To quantitatively assess the wind-induced tracking deviation, the rotation matrices introduced in Section 5.2 are utilized to determine the normal vector of the deviated concentrator which then is compared to the desired normal vector. A projection of the deviated and desired normal vectors to the xz- and yz-plane determines the angular deviations about the y- and x-axis, respectively, which in turn define the wind-induced tracking deviations $\Delta Track_{y,wind}$ and $\Delta Track_{x,wind}$. Fig. 10 depicts the determined wind-induced tracking deviations in time and frequency domain for the evaluated measurement period. An angular deviation about the z-axis (optical axis) does not contribute to the tracking deviation and therefore is not displayed.

Taking the two tracking deviation time courses in Fig. 10a into account, the pronounced mean and background behavior of the Stellio concentrator becomes apparent. During the last third of the measurement period, the concentrator stays deflected about 0.7 mrad for several seconds. The expectation stated in Section 2.1, that the mean and background response is dominant compared to the resonant response, seems valid for the tracking-relevant behavior. A transformation of the tracking deviation courses into frequency domain clarifies this further. The amplitude spectra of the tracking deviations are shown in Fig. 10b. Since the PG data was initially filtered with a lowpass filter and a cutoff frequency of 4 Hz, the amplitude courses above 4 Hz are displayed dashed and are not evaluated.

Firstly taking the frequency range between 2 and 4 Hz into account, distinctive peaks arise in the tracking deviation amplitude spectra, corresponding to the first three eigenfrequencies of the Stellio heliostat. This observation is plausible as the first eigenmodes of a structure are (approximate) rigid body modes. Rigid body modes, in theory, appear as a rotation of the structure around one of its three spatial axes in a stiff manner without any deformations. Hence, the first three eigenmodes of a heliostat are expected to contribute to the tracking deviation significantly. However, it shall be noted that in reality the

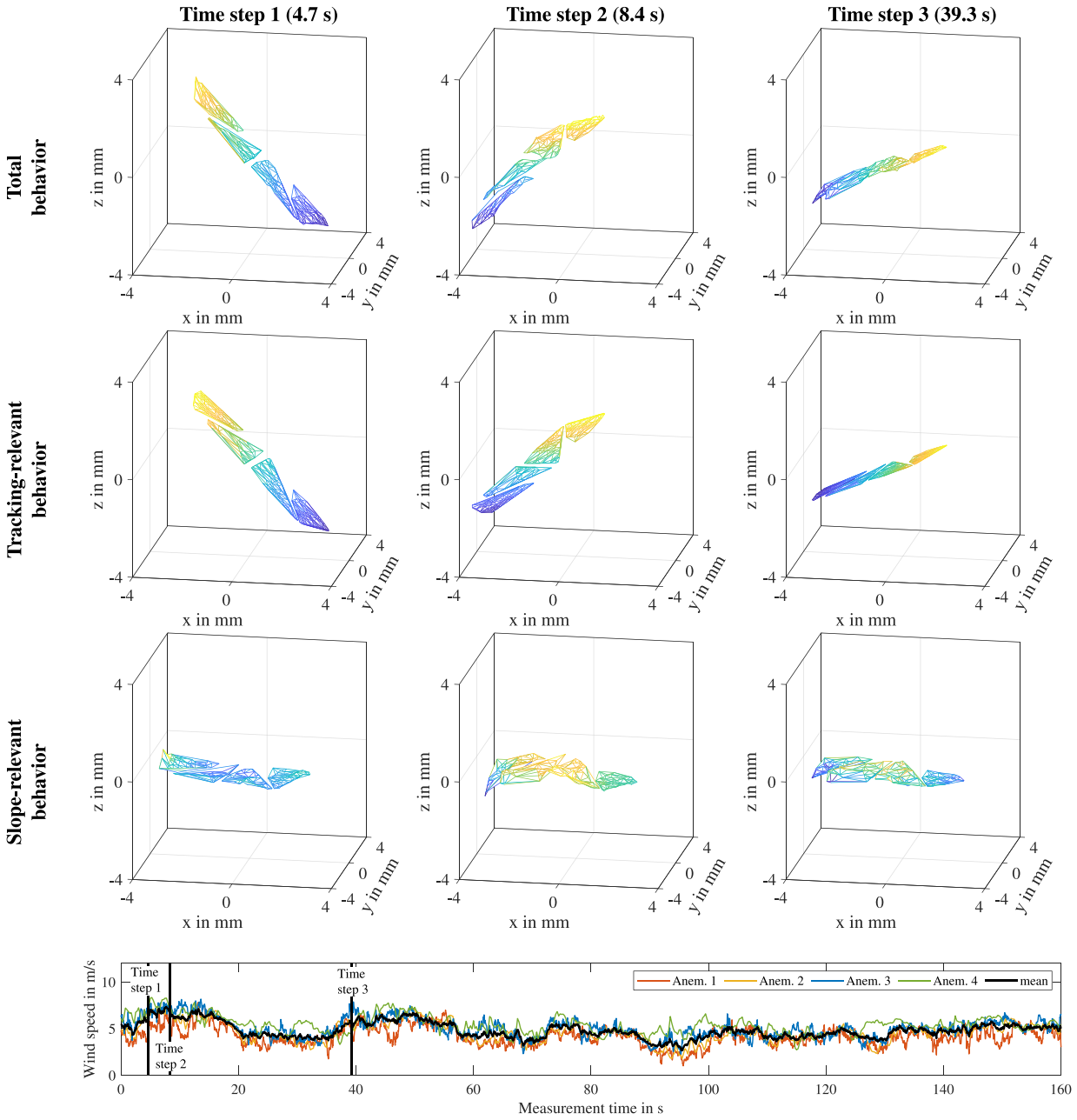

Fig. 9. Top: Visualization of point clouds (i.e. concentrator shapes) for three exemplary time steps captured with dynamic photogrammetry on half of the Stellio concentrator. The point clouds have been scaled from real life scale of the concentrator (meter) to a scale where deformations become visible (millimeter). The coloring of the point clouds does not refer to specific values but is supposed to accentuate the concentrator's deformations and deviations solely. Bottom: Time course of wind speed measured with four anemometers on different heights (see Table 3). Black bars indicate the exemplary time steps.

excitation of rigid body modes can also induce deformations and thus can lead to slope deviations. Regarding the tracking deviation that is related to the range of eigenfrequencies, Fig. 10b clearly illustrates that the amplitudes only reach a tenth or less of such amplitudes within the very low frequency range which corresponds to the mean and background behavior. Table 6 stresses aforementioned finding further and provides a comparison of the RMS values of the tracking deviation separated by its cause, the mean, background and resonant behavior. In conclusion of the previous observations, the RMS values in Table 6 emphasize the predominant contribution of the mean and background behavior to the tracking deviation as their combined RMS values are more than an order of magnitude greater than the resonant related RMS values.

To classify the magnitude of the found wind-induced tracking deviation, a comparison to the total tracking deviation of the Stellio heliostat would be beneficial. As no data is available for the Stellio in particular, a typical RMS value of the total tracking deviation is taken from Röger et al. (2017) where it is mentioned to reach values between 0.8 and 1.6 mrad. The lower value of 0.8 mrad RMS is assumed to represent the total tracking deviation without the impact of wind load. Compared to this value, the found wind-induced RMS tracking deviation of 0.44 mrad, see Table 6, reaches a level of approximately one third[6] of the total RMS tracking deviation.

[6] Comparison of wind-induced tracking deviation to total: $(0.44 \text{ mrad } RMS)^2/(0.8 \text{ mrad } RMS)^2 = 0.3025$.

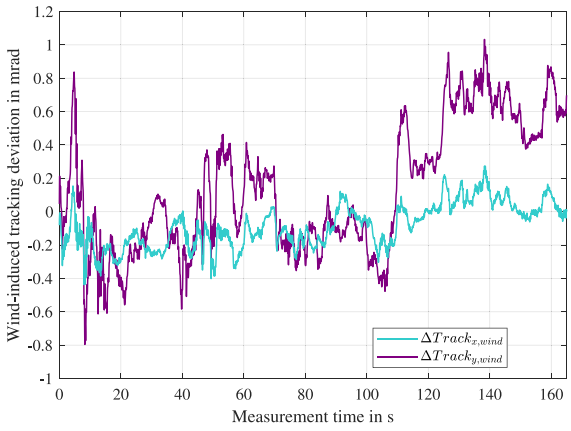

(a) Time domain, the corresponding wind speed is shown in figure 9

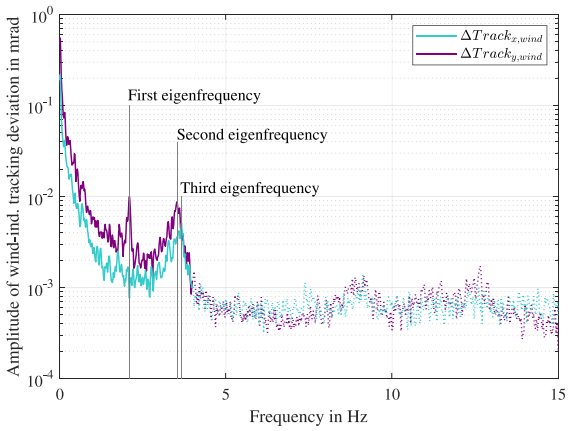

(b) Frequency domain, the range above 4 Hz is displayed dashed as the photogrammetry data was initially filtered with a lowpass filter and a cutoff frequency of 4 Hz

Fig. 10. Courses of wind-induced tracking deviations of the Stellio concentrator obtained from a dynamic photogrammetry measurement.

Table 6
RMS values of wind-induced tracking deviations of the Stellio heliostat obtained from a dynamic photogrammetry measurement separated by their cause, the mean, background and resonant behavior. Comparison of the Stellio wind-induced tracking deviation to typical total tracking deviations of heliostats.

RMS tracking deviation	$\Delta Track_{x,wind}$ in mrad	$\Delta Track_{y,wind}$ in mrad
Mean behavior	0.087	0.134
Background behavior	0.130	0.384
Resonant behavior	0.013	0.022
Wind-induced[a] (Stellio)	≈0.44	
Total (typical)	0.8–1.6	

[a]Total wind-induced RMS value is calculated by means of a quadratic summation of all RMS values, e.g.: $\sqrt{(0.087\ \text{mrad}\ RMS)^2 + (0.130\ \text{mrad}\ RMS)^2} = 0.156\ \text{mrad}\ RMS$.

5.3.2. Impact of wind load on slope deviation

To determine the slope deviation (short: SD) of a dynamic photogrammetry measurement, one single point cloud (in the following termed EVAL point cloud) is compared to a reference point cloud (in the following termed REF point cloud) by means of a Delaunay triangulation. Usually, the REF point cloud represents the ideal concentrator shape and therefore the slope deviation results include all effects that lead to slope deviations, see Section 2.2.2. In contrast, in the framework of this paper, the REF point cloud is not chosen to be the ideal shape but rather to be the least wind-affected actual shape, taken from the period of lowest wind speed, see Section 5.1. In this way, the derived slope deviations solely account for wind-induced effects.

Before carrying out the Delaunay triangulation, an outlier search is applied which checks for implausible deformations between the EVAL and REF point cloud and rejects corresponding points from the evaluation process.[7] Then, the Delaunay triangulation is carried out for the EVAL and REF point cloud respectively, where the discrete points of each cloud are interconnected in such way that a net of non-overlapping triangles results. Next, the orientations of the surfaces, defined by the triangles, are calculated by means of the surface normal vectors. Finally, the deviation between orientations of the EVAL and REF triangles is evaluated and determines the SD.

Figs. 11a and 11b display the spatially distributed wind-induced SDs ($\Delta SD_{rad,wind}$ and $\Delta SD_{tan,wind}$) of the Stellio concentrator for the second time step presented in Fig. 9. Hence, instantaneous values are depicted. As the evaluated time step has been found to exhibit highest deformations, furthermore the maximum wind-induced SDs are depicted that occurred during the investigated measurement period. The slope-relevant shape of this time step (see Fig. 9) revealed strong deformations along the facet corners and edges and according to Figs. 11a and 11b lead to a maximum local $\Delta SD_{rad,wind}$ of −1 mrad and $\Delta SD_{tan,wind}$ of 1 mrad.

In order to understand the cause of wind-induced SDs, Figs. 11c and 11d depict the spatial distribution of $\Delta SD_{rad,wind}$ separated into the mean and background part and the resonant part. This comparison clearly illustrates the predominant contribution of the mean and background behavior to the wind-induced SD. While the excitation of eigenfrequencies and induced deformations related thereto have almost no impact on the wind-induced SD, locally high wind pressures or unsupported, less rigid facet sections can be considered the main cause for mirror deformations and resulting SDs. In case of differently designed and shaped heliostats than the Stellio, however, the impact of wind-excited eigenfrequencies on the SD might not be negligible.

The importance of the identified wind-induced SDs can be classified by comparing them to total SD values. Therefore, the left column in Table 7 states the spatial averages (RMS values) determined from the instantaneous wind-induced SDs of the very left facet, i.e. the most affected facet in Figs. 11a and 11b. The stated wind-induced RMS values are corrected values to account for the impact of PG data noise that increases the SD. Based on our laboratory tests, the noise-induced SD was determined to be 0.12 mrad RMS both in radial and tangential direction. This value was used to correct (decrease) the wind-induced SD determined from the aforementioned most affected facet. In the right column of Table 7, a representative total RMS SD is presented which has been determined through a deflectometry measurement of the Stellio concentrator that takes into account all SD sources except for wind load.[8] The representative total value for a single facet is chosen to be the average of all facets' RMS SDs. While during this study only a single facet was evaluated, it shall be noted that a more common measure of the SD is a global RMS value, representing the entire concentrator. As this value is more widely known, it shall be stated for the Stellio without further elaboration to be 1.37 mrad RMS.

In conclusion, during the investigated measurement period and in consideration of the prevailing wind conditions, the wind-induced RMS

[7] The outlier search is based on (1) identifying neighboring points, (2) fitting a plane through the group of points, (3) determining the deviation of all group points to the plane, (4) rejecting points that deviate more than 1.0–1.5 times the standard deviation of all group's deviations.

[8] The deflectometry measurement was conducted by the company CSP Services, assisted by DLR. Elevation angles of the Stellio concentrator differed during the deflectometry (8°) and dynamic PG measurement (30°).

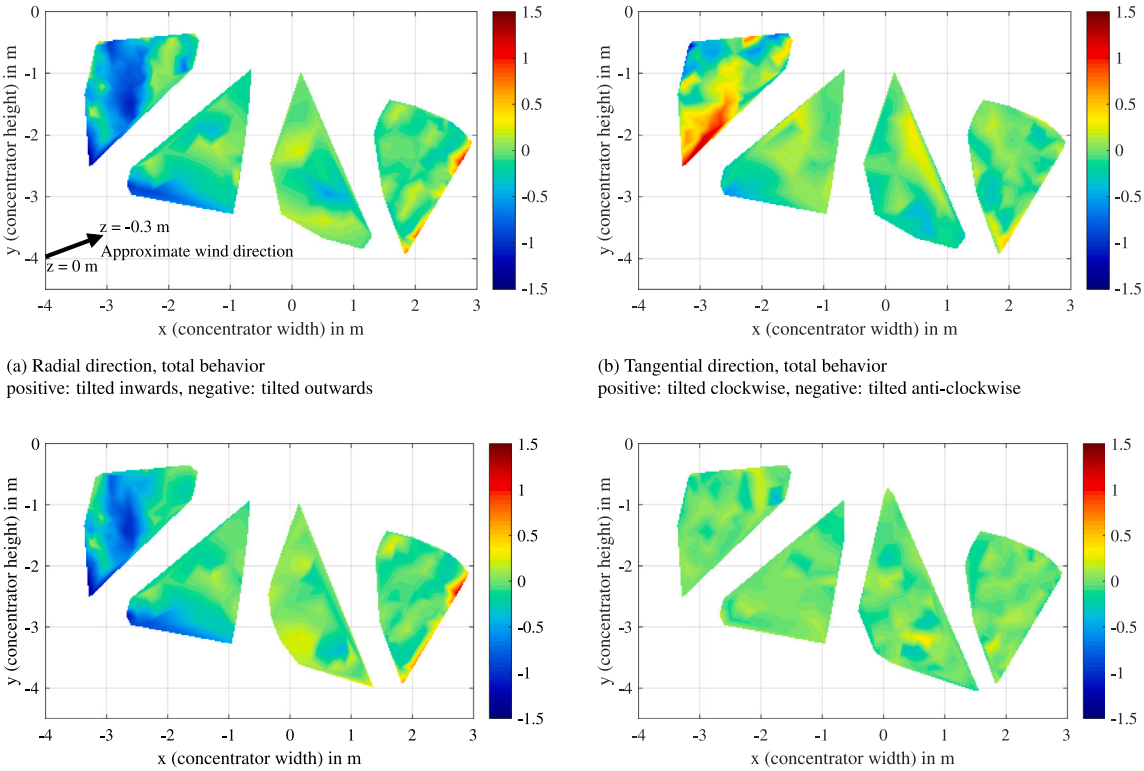

(a) Radial direction, total behavior
positive: tilted inwards, negative: tilted outwards

(b) Tangential direction, total behavior
positive: tilted clockwise, negative: tilted anti-clockwise

(c) Radial direction, mean and background behavior only
positive: tilted inwards, negative: tilted outwards

(d) Radial direction, resonant behavior only
positive: tilted inwards, negative: tilted outwards

Fig. 11. Spatial distribution of the instantaneous wind-induced slope deviations of the Stellio concentrator in mrad, corresponding to time step 2 of Fig. 9. Only four facets are depicted because only the lower half of the concentrator has been investigated. Due to masking effects of the structure and pylon, not all targets had been captured during the measurement period which leads to large gap sizes between the depicted facets. The black arrow indicates the wind direction during the investigated time step.

SD of the most affected facet reached a level of approximately one third[9] of the total RMS SD with regard to Table 7. However, the wind-induced SDs occur only temporally and furthermore only locally.

6. Summary and conclusion

In this study, the wind-induced behavior of a real scale Stellio heliostat and effects on its optical performance were investigated. The wind-induced behavior was captured with a dynamic photogrammetry system which combines a high temporal and a high spatial resolution and allows for detailed insights into the dynamics of a heliostat. Furthermore, a dynamic photogrammetry system, compared to acceleration sensors for example, is well suited to capture heliostat oscillations related to the very low frequency range, below the range of eigenfrequencies. As the dynamic photogrammetry system during this study has been applied to a heliostat for the first time, the applied photogrammetry setup as well as the accuracy of measured displacements was validated at first. Based on the photogrammetry measurements, the effects of wind load on the Stellio concentrator were then qualitatively and quantitatively evaluated. A method was presented which allowed for separating the total wind-induced behavior of the Stellio concentrator into a tracking- and a slope-relevant part in order to study the wind-induced tracking and slope deviation separately.

During the investigated measurement period and with regard to the prevailing wind conditions (mean wind speed: ≈ 4.8 m/s, mean turbulence intensity: ≈ 26%, mean wind direction: ≈ 236°) and to the Stellio orientation (Elevation angle: 45°, Azimuth angle: 160°) the wind-induced tracking deviation (0.44 mrad RMS) was found to reach a level of approximately one third of the typical total tracking deviation of heliostats (0.8 mrad RMS taken from Röger et al. (2017)). Likewise, during the time step of largest deformations, the spatial average of the wind-induced slope deviations (0.75 mrad RMS) of the most affected Stellio facet reached a level of approximately one third of the total slope deviation of a Stellio facet (1.31 mrad RMS). The cause of wind-induced slope deviations was determined to be strong deformations due to locally and temporally occurring high wind pressures or due to unsupported, less rigid facet sections. Furthermore, the excitation of eigenfrequencies was found to have a negligible impact on both the wind-induced tracking and slope deviation. In fact, wind-induced oscillations and deformations related to frequencies below the range of eigenfrequencies were rather found to have a predominant effect on the Stellio heliostat's optical performance.

As it was not part of this study to evaluate the dependency of the tracking and slope deviation on varying wind conditions, further

Table 7
Spatial averages (RMS values) of wind-induced and total slope deviations of a single Stellio facet. Wind-induced RMS values (left column) were determined from the most affected facet (very left one) in Figs. 11a and 11b and at the same time are maximum values found during the investigated period. They have furthermore been corrected (decreased) to account for the impact of noise on the SD. Total slope deviations (right column) result from a deflectometry measurement where the average of all facets' RMS slope deviations is taken as a representative value for a single facet.

RMS slope deviation Stellio single facet	ΔSD_{wind} in mrad	SD in mrad
Radial	0.57	1.03
Tangential	0.49	0.81
Total	0.75	1.31

[9] Comparison of wind-induced slope deviation to total: (0.75 mrad $RMS)^2/(1.31$ mrad $RMS)^2 = 0.3278$.

dynamic photogrammetry measurements will be conducted to investigate the impact of the mean wind speed or the turbulence intensity on the optical performance. Further measurements will not only take the Stellio heliostat into consideration but will be extended to other types of heliostats. As the design of the Stellio heliostat is unique and its mechanical stiffness was optimized, the investigation of different heliostat types will give further insights into wind-induced effects of heliostats.

Declaration of competing interest

The authors declare that they have no known competing financial interests or personal relationships that could have appeared to influence the work reported in this paper.

Acknowledgments

The authors gratefully acknowledge the financial support of the German Federal Ministry for Economic Affairs and Energy (HELIKONTURplus contract 0324053 and Heliodor contract 0324310). Also, the authors would like to thank sbp sonne GmbH for providing and operating the Stellio heliostat, in particular Daniel Nieffer for his technical support. For their valuable comments to the manuscript, the authors would finally like to thank Klaus Pottler from CSP Services GmbH and Gerhard Weinrebe from sbp sonne GmbH as well as the anonymous reviewers.

References

Albert, J., Maas, H.-G., Schade, A., Schwarz, W., 2002. Pilot studies on photogrammetric bridge deformation measurement.

Arbes, F., Weinrebe, G., Wöhrbach, M., 2016. Heliostat field cost reduction by 'slope drive' optimization. AIP Conf. Proc. 1734 (1), 160002. http://dx.doi.org/10.1063/1.4949243.

Balz, M., Göcke, V., Keck, T., von Reeken, F., Weinrebe, G., Wöhrbach, M., 2016. Stellio – development, construction and testing of a smart heliostat. AIP Conf. Proc. 1734 (1), 020002. http://dx.doi.org/10.1063/1.4949026.

Emes, M.J., Arjomandi, M., Ghanadi, F., Kelso, R.M., 2017. Effect of turbulence characteristics in the atmospheric surface layer on the peak wind loads on heliostats in stow position. Sol. Energy 157, 284–297. http://dx.doi.org/10.1016/j.solener.2017.08.031.

Emes, M.J., Jafari, A., Ghanadi, F., Arjomandi, M., 2019. Hinge and overturning moments due to unsteady heliostat pressure distributions in a turbulent atmospheric boundary layer. Sol. Energy 193, 604–617. http://dx.doi.org/10.1016/j.solener.2019.09.097.

Fernández-García, A., Sutter, F., Fernández-Reche, J., Lüpfert, E., 2017. Mirrors. In: Heller, P. (Ed.), The Performance of Concentrated Solar Power (CSP) Systems. Woodhead Publishing, pp. 67–98. http://dx.doi.org/10.1016/B978-0-08-100447-0.00003-1, book section 3.

Gong, B., Li, Z., Wang, Z., Wang, Y., 2012. Wind-induced dynamic response of heliostat. Renew. Energy 38, 206–213. http://dx.doi.org/10.1016/j.renene.2011.07.025.

Gong, B., Wang, Z., Li, Z., Zang, C., Wu, Z., 2013. Fluctuating wind pressure characteristics of heliostats. Renew. Energy 50, 307–316. http://dx.doi.org/10.1016/j.renene.2012.06.037.

Griffith, T.D., Moya, A.C., Ho, C.K., Hunter, P.S., 2015. Structural dynamics testing and analysis for design evaluation and monitoring of heliostats. J. Sol. Energy Eng. 137 (2), http://dx.doi.org/10.1115/1.4028561.

Heller, P., 2017. Introduction to csp systems and performance. In: Heller, P. (Ed.), The Performance of Concentrated Solar Power (CSP) Systems. Woodhead Publishing, pp. 1–29. http://dx.doi.org/10.1016/B978-0-08-100447-0.00001-8, book section 1.

Ho, C.K., Griffith, T.D., Sment, J., Moya, A.C., Christian, J.M., Yuan, J.K., Hunter, P.S., 2012. Dynamic testing and analysis of heliostats to evaluate impacts of wind on optical performance and structural fatigue. In: 18th SolarPACES Conference. Marrakech, Morocco.

Holmes, J.D., 2015. Wind Loading of Structures, Vol. 3. CRC Press, Boca Raton, http://dx.doi.org/10.1201/b18029.

Nieffer, D., Effertz, T., Macke, A., Röger, M., Weinrebe, G., Ulmer, S., 2019. Heliostat testing according to solarpaces task iii guideline. AIP Conf. Proc. 2126 (1), 030039. http://dx.doi.org/10.1063/1.5117551.

Peterka, J.A., Tan, Z., Cermak, J.E., Bienkiewicz, B., 1989. Mean and peak wind loads on heliostats. J. Sol. Energy Eng. 111 (2), 158–164. http://dx.doi.org/10.1115/1.3268302.

Pfahl, A., Buselmeier, M., Zaschke, M., 2011. Wind loads on heliostats and photovoltaic trackers of various aspect ratios. Sol. Energy 85 (9), 2185–2201. http://dx.doi.org/10.1016/j.solener.2011.06.006.

Pfahl, A., Uhlemann, H., 2011. Wind loads on heliostats and photovoltaic trackers at various Reynolds numbers. J. Wind Eng. Ind. Aerodyn. 99 (9), 964–968. http://dx.doi.org/10.1016/j.jweia.2011.06.009.

Pottler, K., Lüpfert, E., Johnston, G., Shortis, M., 2004. Photogrammetry: A powerful tool for geometric analysis of solar concentrators and their components. J. Sol. Energy Eng. 127, http://dx.doi.org/10.1115/1.1824109.

Pottler, K., Mützel, M., Engelke, J., Prahl, C., Röger, M., 2011. QFoto: Automatic inline measurement system for parabolic trough structures: Experiences and development. In: 17th SolarPACES Conference. Granada, Spain.

Röger, M., Prahl, C., Pernpeintner, J., Sutter, F., 2017. New methods and instruments for performance and durability assessment. In: Heller, P. (Ed.), The Performance of Concentrated Solar Power (CSP) Systems. Woodhead Publishing, pp. 205–252. http://dx.doi.org/10.1016/B978-0-08-100447-0.00007-9, book section 7.

Vasquez Arango, J.F., 2016. Dynamic Wind Loads on Heliostats (Thesis). Rheinisch-Westfälische Technische Hochschule Aachen, http://dx.doi.org/10.18154/rwth-2016-12225.

Wu, Z., Gong, B., Wang, Z., Li, Z., Zang, C., 2010. An experimental and numerical study of the gap effect on wind load on heliostat. Renew. Energy 35, 797–806. http://dx.doi.org/10.1016/j.renene.2009.09.009.